Bulletin of the *Transilvania* University of Braşov
Series III: Mathematics and Computer Science, Vol. 6(68), No. 1 - 2026, 237-254
https://doi.org/10.31926/but.mif.2026.6.68.1.16

MULTISPECTRAL IMAGE VISUALIZATION AND NDVI-BASED ANOMALY DETECTION

Alexandra BĂICOIANU[1], Mihai IVANOVICI[2] and Ioana Cristina PLAJER[*,3]

Abstract

Satellite imagery is essential for advancing precision agriculture, providing the foundation for accurate monitoring and decision-making. A key initial step in analyzing multispectral images is achieving a visualization that accurately reflects real-world conditions. Effective visualization mechanisms, such as those driven by Machine Learning (ML), depend on the availability of well-structured datasets. This study investigates how characteristics such as the quantity, variability, and quality of datasets influence the quality of visualization outcomes. Our findings highlight that data quantity and variability are more critical than quality in achieving optimal results. The research also explores the use of standard Macbeth color charts to improve dataset consistency in spectral analysis. Additionally, we propose a straightforward and computationally efficient methodology for interpreting and analyzing multispectral images in the context of anomaly detection. Using the Normalized Difference Vegetation Index (NDVI), this approach enables automatic identification of potential crop development issues, offering practical benefits for agricultural health monitoring and early intervention strategies. By addressing the challenges of data availability and proposing an anomaly detection methodology, this study provides valuable insights into the use of satellite imagery for monitoring and improving agricultural practices. These findings contribute to the broader understanding of optimizing satellite imagery analysis for agricultural applications.

2000 *Mathematics Subject Classification:* 68U10, 68T07, 68U05, 68T01.

Key words: multispectral images, Macbeth color chart, fully connected NN, NDVI, anomalies.

[1]Faculty of Mathematics and Computer Science, *Transilvania* University of Braşov, Romania, e-mail: a.baicoianu@unitbv.ro

[2]Faculty of Electronics and Computers, *Transilvania* University of Braşov, Romania, e-mail: mihai.ivanovici@unitbv.ro

[3]* *Corresponding author*, Faculty of Mathematics and Computer Science, *Transilvania* University of Braşov, Romania, e-mail: ioana.plajer@unitbv.ro

1 Introduction

In recent years, the increasing public availability of satellite data has significantly expanded the role of Earth Observation (EO) across various research fields. Satellite information is no longer limited to military and security applications [2], [10], [26], it now underpins critical solutions in areas such as environmental monitoring [5], [36], urban planning [33], [35], forestry management [14], [25], disaster response [1], [15], or precision agriculture [21], [32]. With the growing availability and advancement of remote sensing technologies, researchers and practitioners can now capture detailed data across diverse landscapes spectra, and time frames. This has led to valuable applications across fields such as environmental monitoring, agriculture, urban planning, and disaster management. The practical insights gained from multispectral and other types of EO data enable accurate detection of land use changes, assessment of vegetation health, and real-time response in emergency situations. As interpretation methods advance, EO remains essential for addressing global challenges, from resource management to disaster resilience and urban planning.

Precision agriculture aims at optimizing the resources needed for food production while increasing the quantity and quality of crops. This can be done by efficient monitoring [11], rapid and precise intervention in case of plant diseases or growth problems [38], and prediction of different parameters. In addition, Agriculture 5.0 leverages Artificial Intelligence to accelerate the processing and utilization of EO data.

Multispectral (MS) and hyperspectral (HS) images acquired by sensors embarked on various satellites, capture a series of spectral bands, which often exceed the domain of visible light ([400 - 700 nm]), thus offering significant information, outside what can be visually perceived. The near-infrared (NIR) bands, permit estimating vegetation growth and health, or soil moisture [17], [30], [37]. The short wave infrared provides information about ice, clouds, and other features. The range and number of bands captured by satellites can vary significantly, from a few, such as Sentinel-2 (12) or Landsat (8,10), to hundreds in the case of hyperspectral satellites, like the PRISMA or AVIRIS.

The initial step of interpretation for spectral images involves human visual inspection. To facilitate this process, images containing numerous spectral bands must be adapted to a 3-channel RGB format, allowing for visualization on standard digital displays. A large number of such mapping algorithms have been developed, starting from basic band selection [13], [28], to feature-based PCA [12]. More recently neural network based like [7], [23] have offered more realistic and qualitative results. Machine Learning (ML) models rely on well-structured datasets for effective training, yet obtaining such data in remote sensing is challenging. Limited access to labeled data, along with variations in environmental conditions and sensor types, can hinder the creation of comprehensive, high-quality datasets. These constraints often impact the accuracy and generality of ML models in remote sensing applications.

Satellite images are important in smart agriculture, especially in the early

detection of issues and crop health problems. Within precision agriculture, utilizing anomaly detection techniques on multi and hyperspectral imagery can play a pivotal role in improving crop productivity, reducing environmental impact, and advancing sustainable and efficient farming practices [29], [3]. The choice between classical and advanced methods often depends on the acquired data and the type of sensors, the anomalies' complexity, and the available resources, such as computational power, specialized software, expert knowledge, financial budget, and time constraints. While classical methods may be sufficient for certain applications [40], [31], advanced methods, particularly those based on ML and deep learning [6], [4], offer the advantage of adaptability to complex patterns and the ability to handle high-dimensional data, such as hyperspectral imagery, more effectively.

An essential aspect of crop monitoring is the quick detection of issues related to crop health and growth, specifically identifying areas that deviate from the typical expected growth pattern. We can consider such regions as anomalies, transforming the task into an anomaly detection problem.

Spectral images in a raw state are usually large volumes of data and the different bands contain a lot of information, which is not significant for crop monitoring, or which may be redundant. Therefore, a series of vegetation indices [27], adapted to specific tasks, were developed. The Normalized Difference Vegetation Index (NDVI) [20] is a widely used vegetation index and a robust indicator, which offers information over land cover and vegetation health. Our approach involves the utilization of NDVI maps in order to effectively identify areas exhibiting abnormal NDVI values and signal potential health concerns in the targeted agricultural zones.

Visual interpretation and analysis of multispectral images are crucial to extracting meaningful insights from remote sensing data. This study addresses two key aspects of this process. First, it explores the methods for achieving optimal visualization of spectral images and investigates how the choice of dataset influences this visualization when using neural networks (NNs). Second, the study proposes a simple, but very effective approach for detecting anomalies in NDVI maps derived from multispectral images, further enhancing the interpretation of crop health and growth patterns.

2 Materials and methods

This section outlines the data and methodologies employed in our study to ensure consistent and accurate visualization of spectral images, as well as to analyze anomalies in NDVI maps. First, the datasets are described, followed by an overview of the techniques for color image rendering and visualization. Next, the methodology for anomaly detection in NDVI maps is detailed, highlighting the approach implemented to identify deviations from expected patterns. These methods are essential for the effective interpretation and analysis of multispectral images, supporting the overall objectives of the study.

2.1 Color image rendering and visual interpretation

(a) (b)

(c) (d)

Figure 1: a) 8-color chart, b) 24-color Macbeth chart, c) RGB visualization of the 8-color-chart acquired hyperspectral image, d) RGB visualization of the 24-color-chart acquired hyperspectral image.

As discussed earlier, multispectral and hyperspectral images cannot be directly displayed on standard digital devices. To enable human users to visually interpret these images and provide an initial layer of validation, it is necessary to apply a color mapping technique that converts the spectral data into an color RGB image that closely represents the natural scene captured by the sensor.

Various algorithms for this task are described in literature, ranging from simple methods, such as classical band selection, to more sophisticated approaches like the multichannel pulse-coupled neural network (MPCNN) [8]. Each approach has its own advantages and limitations, and the resulting images often require additional pre- or post-processing to ensure proper brightness, contrast, and realistic color reproduction. Recent research has demonstrated that NNs can produce superior results [23]. NNs offer a distinct approach to visualization, as they can learn from all spectral bands, are robust to data outliers, adapt to varying resolutions, and generate images that typically do not require post-processing.

Datasets for visualization

An appropriate dataset is essential for applying a ML approach to image visualization. Such a dataset must include an RGB image for each spectral image in

the set, enabling the mapping of spectral pixels to RGB triplets. Currently, very few datasets for this purpose are publicly available. The most widely known are the CAVE dataset [34] and the UGR dataset [9].

The CAVE dataset contains 32 images of indoor scenes with a resolution of 512×512 pixels. The spectral resolution is 10 nm, with the acquired wavelengths in the visible range, spanning [400 nm - 700 nm]. The resulting MS images dispose thus of 31 spectral channels. The UGR dataset contains 14 images of urban scenes, acquired in outdoor conditions with a spectral resolution of 10 nm, with 61 bands wavelength in the interval [400 nm - 1000 nm]. The spatial resolution is 1000×900, respectively 900×1000 pixels. Both datasets were used in successfully training a fully connected neural network (FCNN) for image visualization [23].

Given the limited availability of datasets, the focus of this study was on constructing a new, carefully designed dataset aimed at accurately representing the colors from the Macbeth color charts.

Constructing a dataset from the Macbeth Color Chart

Color				
RGB label	(0,0,255)	(0,255,255)	(0,255,0)	(255,255,0)
Color				
RGB label	(255,0,0)	(255,0,255)	(255,255,255)	(0,0,0)

Table 1: Colors and corresponding labels of the 8-color chart.

The Macbeth color chart represents a standard color calibration target which allows accurate matching between multispectral pixels and RGB colors. There exist two charts, a smaller one with 8 colors corresponding to the corners of the RGB cube, and a larger one, with 24 colors which have spectral reflectances intended to mimic those of natural objects such as human skin, foliage, and flowers. The charts are represented in Figure 1. As the colors in the charts were calibrated to correspond to natural colors, we assumed, they should provide better visualization results of the proposed FCNN [23].

In order to construct a dataset using the Macbeth charts, spectral images of the charts were acquired with a portable SPECIM IQ HS camera with a high spectral resolution (204 bands) in controlled laboratory conditions. The RGB visualization of the acquired images is presented in Figures 1c and 1d. Two small datasets, one for each chart, were constructed from these HS images by manually selecting small areas inside each colored rectangle. The dataset from the 8-color chart contains 3,704 HS pixels and 8 labels (corresponding to the 8 colors), while the dataset from the 24-color chart contains 12.168 HS pixels and 24 labels (corresponding to the 24 colors). The labels were produced, by specifying the exact RGB color coder corresponding to the selected rectangles. The labels for the 8-color chart

Color				
RGB label	(115,82,68)	(194,150,130)	(98,122,157)	(87,108,67)
Color				
RGB label	(133,128,177)	(103,189,170)	(214,126,44)	(80,91,166)
Color				
RGB label	(193,90,99)	(94,60,108)	(157,188,64)	(224,163,64)
Color				
RGB label	(56,61,150)	(70,148,73)	(175,54,60)	(231,199,31)
Color				
RGB label	(187,86,149)	(8,133,161)	(243,243,242)	(200,200,200)
Color				
RGB label	(160,160,160)	(122,122,122)	(85,85,85)	(52,52,52)

Table 2: Colors and corresponding labels of the 24-color MabBeth chart.

are presented in Table 1, while the labels for the 28-color chart are illustrated in Table 2.

Model architecture

The fully-connected neural network described in [23] features a simple five-layer architecture and was originally designed for training on the CAVE and UGR datasets, which contain 31 wavelengths in the visible spectrum. Given that the HS images in this study include 204 spectral bands, the network had to be modified to accommodate this input, leading to the architecture presented in Table 3.

Layer	**Number of neurons**
Input layer	204 (corresponding to the input spectral bands)
Hidden layer 1	128
Hidden layer 2	64
Hidden layer 3	32
Hidden layer 4	8
Output	3 (corresponding to RGB)

Table 3: Layers and number of neurons.

The number of neurons in the input layer corresponds to the number of wave-

lengths, i.e. channels, present in the spectral images. This number was selected to fit the spectral bands of the training set. The FCNN was trained first on the 8-color chart and then on the 24-color one, using the same methodology and preprocessing algorithm as in [23]. The trained network was used for image visualization of HS images acquired by the PRISMA satellite. The results are shown in Section 3 and compared with classical methods and the results obtained by the FCNN presented in [23].

Visualizing spectral images serves as a preliminary step for analysis. To extract meaningful information from the data and leverage the content of the various spectral bands, it is essential to select appropriate methods for analysis and interpretation. Given that our study focuses on agricultural applications, the primary emphasis is on methods relevant to this field. Therefore, the next subsection will introduce the key concepts used in this context.

2.2 Analysis of anomalies in NDVI maps

A major concern in precision agriculture is the early detection of issues and diseases affecting crops. A promising approach is anomaly detection in satellite images of agricultural parcels. The present study uses NDVI maps to find regions with anomalous NDVI values, which could indicate health risks in specific agricultural zones and highlights the importance of performing a local analysis of NDVI values in a neighborhood in order to identify affected areas in apparently healthy regions.

The NDVI is a vegetation index, computed from the red (RED) and near-infrared (NIR) spectral bands of the MS image by the general formula, see Equation 1.

$$NDVI = \frac{NIR - RED}{NIR + RED} \tag{1}$$

The values of the NDVI are in the range $[-1, 1]$, with the following interpretation: $[-1, 0]$ for water or in-animated objects; $(0, 0.33]$ for bare soil with little to no vegetation cover; $(0.33, 0.66]$ for unhealthy or sparse vegetation; $(0.66, 1]$ for dense and healthy vegetation. For the definition of anomalies, we consider the NDVI values computed for each pixel, based on the multi- or hyper-spectral information, can fall in the fore-mentioned intervals, which correspond to the specific interpretation from the point of view of the crop vegetation stage and health status (see Table 4). We exclude the interval $[-1, 0]$ which is not of interest for agriculture, as it corresponds to artificial and water surfaces.

NDVI	**Interpretation**
[0,0.33]	dead/dried/underdeveloped vegetation
[0.33, 0.66]	moderately healthy/developed vegetation
[0.66, 1]	very healthy/developed vegetation

Table 4: NDVI intervals and interpretation.

In this study, we aim at identifying anomalous areas in agricultural crops, in the NDVI maps computed based on multi-spectral or hyper-spectral images. We highlight the importance of early anomaly detection in agriculture for the purpose of improving the general health and productivity of agricultural landscapes.

In the context of our study, we define an anomaly as a pixel with an NDVI below a certain threshold (indicating a moderately healthy or underdeveloped crop), surrounded by pixels of healthy vegetation (with values above the chosen threshold). We define the following two types of anomalies that can occur in NDVI maps, in 3×3 pixel vicinities, illustrated in Figure 2a yellow pixels, with NDVI values between 0.33 and 0.66, surrounded by green pixels, with NDVI values comprised between 0.66 and 1 and in Figure 2b red pixels, with NDVI values between 0 and 0.33, surrounded by green pixels, with NDVI values comprised between 0.66 and 1. The definitions of anomalies are based on the assumption that in normal conditions, the agricultural crops should develop consistently over the seeded area, consequently neighbour pixels in a given vicinity, in our case 3×3, should all be in the same NDVI intervals. A yellow or red pixel surrounded by green pixels may be an indication of some anomaly affecting that corresponding area.

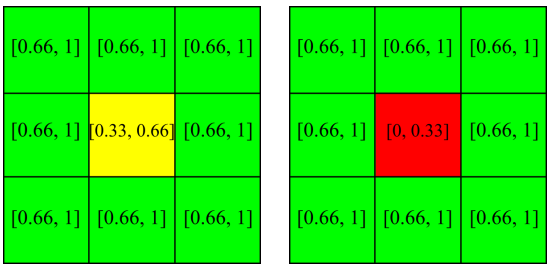

(a) (b)

Figure 2: Anomaly definition in NDVI maps.

With this definition of an anomaly, in the considered image, we looked for 3×3 neighborhoods where the central pixel had an NDVI below 0.66, and all its eight neighbors had values above this threshold. According to the given definition, an anomaly can occur even in areas where the central pixel, although below the threshold of 0.66, might be very slightly different from its neighbors, which have values above this threshold. Thus, in Section 3, we studied this aspect in order to identify the parcels with a high probability of representing an anomaly.

3 Experimental results and discussions

In this section we will present the qualitative and quantitative results of the two problems discussed in this study: the visualization of spectral images, using an appropriate dataset, and the analysis from the point of view of anomalies in NDVI maps.

3.1 Impact of the dataset size, variability and quality on image visualization

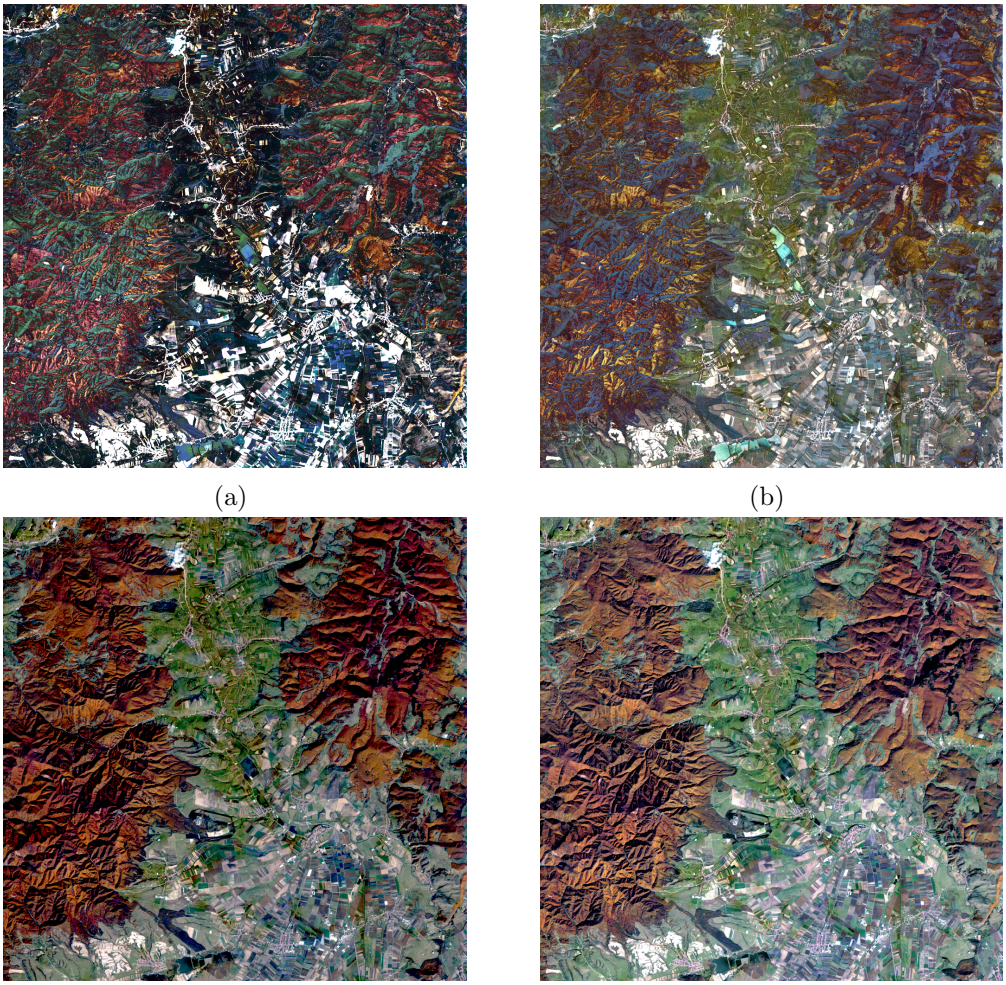

(a) (b) (c) (d)

Figure 3: PRISMA HS image visualized with a FCNN trained: a) on 8-color chart; b) on 24-color chart; c) on CAVE dataset [23]; d) on UGR dataset [23].

In order to obtain a qualitative and color consistent visualization for the spectral images, we extended the experiments presented in [23], as described in Section 2. The visualization was performed using a FCNN trained on the datasets constructed from the color charts presented in Section 2 on a HS image acquired by the PRISMA satellite over Braşov county in October 2022. The PRISMA satellite was launched by the Italian Space Agency and the HS images acquired have 239 spectral bands, spanning from 400 nm to 2500 nm with a spectral sampling of less than 12 nm. The spatial resolution is of 30 m. We considered for visualization only the 66 which fall within the Visible Near Infra-Red range [400 nm - 1010 nm]. As the number of bands and the wavelengths differ from those of our training set,

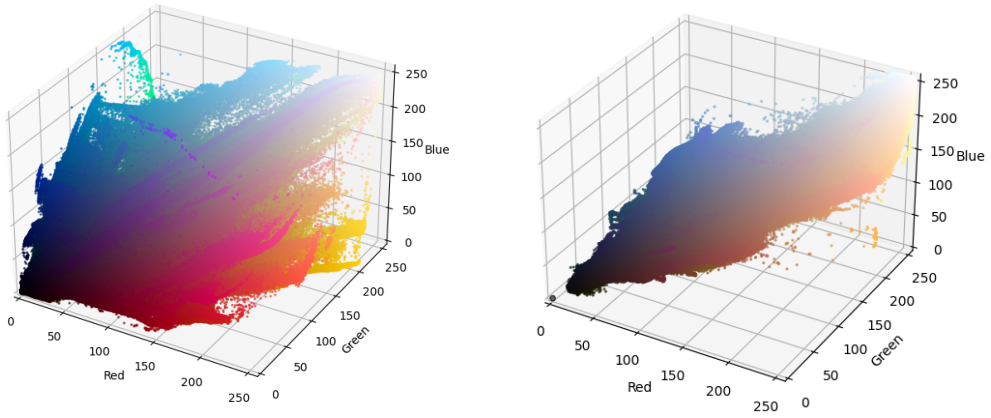

(a) (b)

Figure 4: a) 3D Histogram of RGB colors present in the CAVE dataset; b) 3D Histogram of RGB colors present in the UGR dataset.

the images were first interpolated, as to adapt to the input of the FCNN, and then each pixel was fed to the network, in order to be mapped onto an RGB value.

As can be seen from Figure 3, the results of the network trained on the chart-datasets are not as qualitative, as expected. Although the spectral image samples and the corresponding labels were constructed with care, and the colors are very precise, the results are worse, than in the case of the FCNN presented in [23], trained on the publicly available CAVE and UGR datasets. However, the small number of colors in the training set leads to a strong color quantization effect in the resulting image (which could be useful for a further compression and segmentation step).

Sample	**BRISQUE** [18]	**IQA by ResNet50**	**Color-based IQA** [39]
FCNN/UGR	**4.469**	3.472	**4.3822**
FCNN/CAVE	4.381	**3.487**	4.3364
FCNN/8-colors	3.643	3.330	4.0716
FCNN/24-colors	3.907	3.261	4.1199

Table 5: Results of blind IQA assessment methods for FCNNs trained with the 4 datasets. The evaluation scores are in the range of [1, 5], where 5 is for the best quality.

Both the visual results and the quantitative ones, assessed using classical image quality measures (IQA) as shown in Table 5, reflect this situation.

We analyzed the causes of this problem and compared the considered datasets from different points of view. On one hand, as we can see in Table 6, the size of the datasets can be one of the causes. While the CAVE and UGR datasets contain millions of pixels in their images, the datasets constructed using the color

Dataset	**No. of pixels**	**No. of RGB distinct colors**
CAVE	8.388.608	1.375.879
UGR	12,600,000	697,153
Macbeth 8 colors	3,704	8
Macbeth 24 colors	12,168	24

Table 6: Size and variability of the 4 datasets.

charts contain significantly fewer pixels. However the most significant limitation is in the variability of these datasets. While UGR and CAVE RGB image labels exhibit over 600.000, respectively over 1 million colors, the charts dispose of only 8, respectively 24 different labels. Although the colors in the two small datasets are well calibrated, the FCNN cannot correctly generalize from the few basic colors present, the large number of other intermediate ones. Furthermore, if we compare UGR and CAVE datasets, we can observe, that the latter exhibits a larger number of colors and a better spread across the RGB cube, as can be seen in the 3D histograms of the colors presented in Figure 4.

3.2 Anomalies in NDVI maps

We have conducted a series of experiments aiming to achieve our goal of anomaly detection in NDVI maps. This section thoroughly outlines the outcomes obtained and offers nuanced interpretations.

The hyperspectral image used in our experiments was obtained from the Italian Space Agency (ASI)'s PRISMA satellite on 24 March 2023 over a region of Braşov county. Images collected by the PRISMA satellite cover a range of 239 spectral bands, from 400 to 2500 nm, with 66 bands in the visible and near-infrared (VNIR) and 173 in the short wave infrared (SWIR) domains. The sampling interval for the spectral bands is smaller than 12 nm, thus providing a significant amount of information. The resolution of the PRISMA image is 1000×1000, with a spatial resolution of 30m. The PRISMA satellite provides 4 product levels of the raw image, with different types of correction. The product used in this study is the *L2C level*, comprising atmospheric correction.

Figure 5a presents a visualization of the PRISMA image where this was performed by a FCNN trained on the CAVE dataset offering a significant color diversity in the visible domain [22].

In literature, there are a variety of color palettes [19] to represent the NDVI map, as discussed in [24]. The four-color palette shown in Figure 5c which corresponds to the 4 intervals described in Section 2, was used to generate the NDVI map for the PRISMA image. The map is shown in Figure 5b, where the wavelengths used to compute the NDVI formula from Equation (1) were 665 nm for RED, and 839 nm for NIR as discussed in [24].

Based on the definition of an anomaly given in Section 2, we identified 646 anomalies in the PRISMA image. Figure 6 shows four magnified samples of agricultural parcels with anomalies highlighted in magenta.

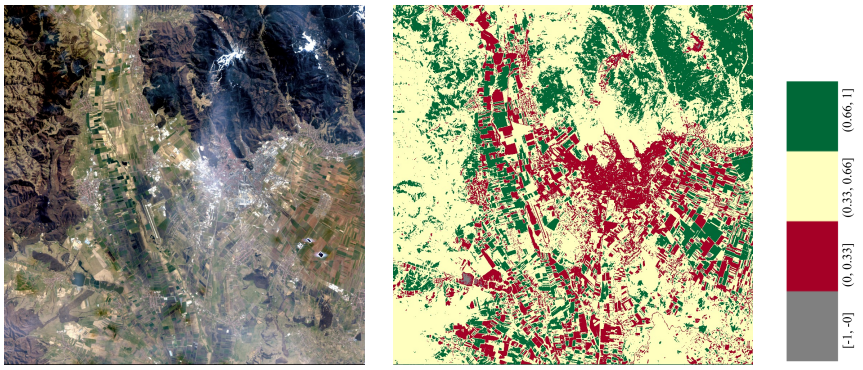

(a) (b) (c)

Figure 5: a) Original PRISMA image RGB visualization; b) its corresponding NDVI map; c) NDVI color palette.

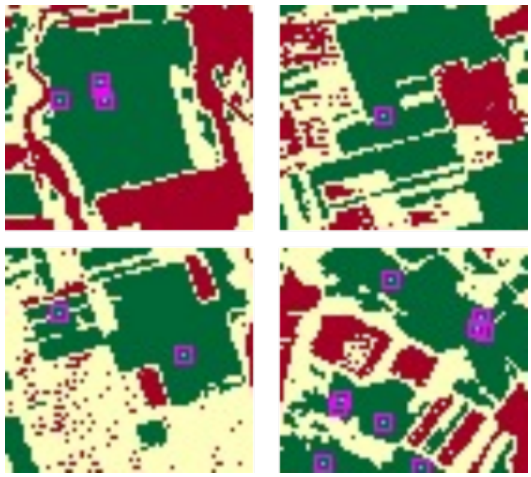

Figure 6: Zoom in image crops with detected anomalies (marked with magenta).

Following the detection, we aimed to understand the spread of the anomalies in a Red-NIR diagram representation. In Figure 7a we represented all pixels in the PRISMA image, as pairs of the values of the red and NIR wavelengths, using colors from the specified color palette. In blue, we highlight the points that represent the detected anomalies. One can notice that the blue anomalous spots are situated on the border between the green and yellow points, indicating pixels that are *migrating* from the green to the yellow regions. Basically, the detected anomalies are pixels that may fall into the following two categories:

1. pixels that were green and recently moved to the yellow region (one possible interpretation is that the corresponding agricultural crop is lacking water or nutrients and the corresponding alarms should be generated) or

2. pixels that are yellow and they will move to green (one possible interpretation is that the vegetation is growing, so the moderately-developed agricul-

tural crop will turn into well-developed vegetation).

The anomalies can only be confirmed by analyzing the evolution of the pixels in time by analyzing a time series.

There are anomalies that are more relevant to monitor and interpret, namely those in which the value of the central pixel is significantly smaller than the threshold of 0.66, indicating a problematic region. The expectation is that these regions are represented by the spots in Figure 7a that are included in the yellow area. However, the difference between the green and yellow pixels may be very small due to noise in the acquisition process. In order to study the relevance of the detected anomalies, we examined how many anomalies have all neighbors significantly different from the central pixel, we determined the number of neighbors of central pixels with values higher than the central one by a certain value. Various thresholds for this value were considered, and the results are presented in the histograms of Figure 7b.

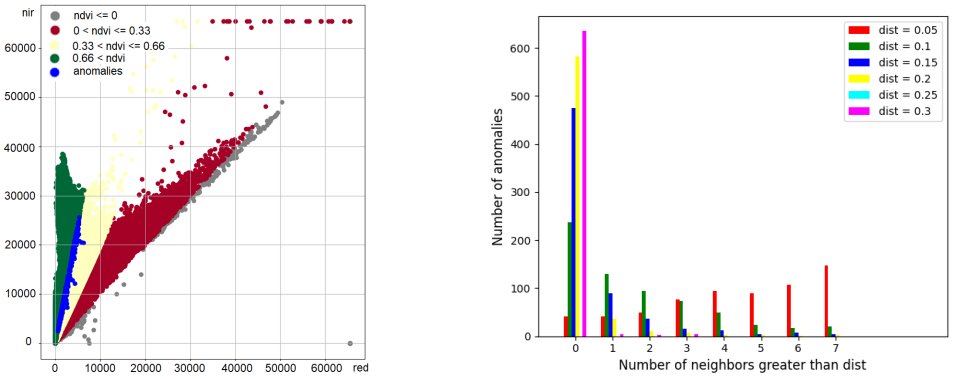

(a) (b)

Figure 7: a) Red and NIR values for the pixels in PRISMA image, with highlighted anomalies in blue. b) Histograms of anomaly differences.

As shown in Figure 7b, the number of anomalies with significant differences between the central pixel and its neighbors is small. Less than 10% of the blocks exhibit differences greater than 0.1 between the central pixel and its neighbors. Consequently, anomalies with statistically significant differences are rare.

By studying the distribution of NDVI values in the image and the local variance of NDVI for 3×3 neighborhoods, we observed that certain neighborhoods exhibited unusually high variance, indicating possible anomalies. Interestingly, these regions also showed unusual values when the image was visualized using the neural network we trained. Upon examining the region on Google Maps, we identified that these areas correspond to regions where solar panels were installed. These panels reflect solar radiation in a completely different manner than vegetation, leading to the appearance of abnormal values. The image section containing the solar panels and its NDVI, together with the identified anomalies are presented

(a) (b)

Figure 8: a) The anomalies in the NDVI; b) color RGB composite of the PRISMA image section containing the solar panels.

in Figure 8.

4 Conclusions

Multispectral and hyperspectral satellite images, now widely accessible through various space missions, like Sentinel-2 or PRISMA, provide a valuable and cost-effective tool for precision agriculture, such as crop monitoring and plant health assessment. It is crucial thus, to correctly and effectively analyze such images, with the first step often being visual inspection by human users. In this context, providing a natural visualization of spectral images in the RGB color space - a standard for digital devices - is of great importance. Neural networks, which are well-suited for this task, require high-quality datasets to achieve optimal results. Our study examined the impact of dataset quality and variability on the performance of an FCNN used for visualization. The results showed that the quantity of data has a greater influence on model generalization than the precision of the labels provided by the Macbeth color charts.

The second aspect addressed after the visualization problem is the use of satellite data for image analysis in the context of anomaly detection. This article proposes a method that is both algorithmically simple and computationally efficient for identifying potential anomalies in plant development, based on a standard vegetation index from the specialized literature, namley the NDVI. Currently, this methodology relies on single image analysis, but in future research, we aim to validate the method using time series data and in-situ measurements.

Based on a series of experiments, we provide comprehensive findings and nuanced interpretations of anomaly identification in NDVI maps. In addressing crop health issues, the article emphasizes the need for rapid detection and response and the importance of conducting a single-shot analysis designed especially for a given crop in agriculture.

Acknowledgments

Funded by the European Union. The AI4AGRI project entitled "Romanian Excellence Center on Artificial Intelligence on Earth Observation Data for Agriculture" received funding from the European Union's Horizon Europe research and innovation program under grant agreement no. 101079136.

The hyperspectral image from the PRISMA satellite presented in this paper was kindly provided by the Italian Space Agency (ASI).

References

[1] Al Shafian, S. and Hu, D., *Integrating machine learning and remote sensing in disaster management: a decadal review of post-disaster building damage assessment*, Buildings **14** (2024), no. 8, 2344.

[2] Avtar, R., Kouser, A., Kumar, A., Singh, D., Misra, P., Gupta, A., Yunus, A. P., Kumar, P., Johnson, B. A., Dasgupta, R. et al., *Remote sensing for international peace and security: its role and implications*, Remote Sens. **13** (2021), 439.

[3] Basener, W. F. and Messinger, D. W., *Enhanced detection and visualization of anomalies in spectral imagery*, Algorithms and Technologies for Multispectral, Hyperspectral, and Ultraspectral Imagery XV. Proc. of SPIE 7334, Orlando, Florida, USA, April 13-17, 2009 (Eds. Shen, Sylvia S. et al.), Bellingham, SPIE, 621-630, 2009.

[4] Chang, C.-I. and Chiang, S.-S., *Anomaly detection and classification for hyperspectral imagery*, IEEE Trans. Geosci. Remote Sens. **40** (2002), 1314-1325.

[5] Chuvieco, E., *Fundamentals of satellite remote sensing: an environmental approach*, CRC Press, 2020.

[6] Coca, M. and Datcu, M., *Anomaly detection in post fire assessment*, 2021 IEEE International Geoscience and Remote Sensing Symposium. Proc. of IGARSS 2021, Brussels, Belgium, July 11-16, 2021, IEEE, 8620-8623, 2021.

[7] Duan, P., Kang, X. and Li, S., *Convolutional neural network for natural color visualization of hyperspectral images*, 2019 IEEE International Geoscience and Remote Sensing Symposium. Proc. of IGARSS 2019, Yokohama, Japan, July 28 - August 2, 2019, IEEE, 3372-3375, 2019.

[8] Duan, P., Kang, X., Li, S. and Ghamisi, P., *Multichannel pulse-coupled neural network-based hyperspectral image visualization*, IEEE Trans. Geosci. Remote Sens. **58** (2019), no. 4, 2444-2456.

[9] Eckhard, J., Eckhard, T., Valero, E. M., Nieves, J. L. and Contreras, E. G., *Outdoor scene reflectance measurements using a Bragg-grating-based hyperspectral imager*, Appl. Opt. **54** (2015), no. 13, D15-D24.

[10] Kaplan, G., Rashid, T., Gasparovic, M., Pietrelli, A. and Ferrara, V., *Monitoring war-generated environmental security using remote sensing: a review*, Land Degrad. Dev. **33** (2022), no. 10, 1513-1526.

[11] Karmakar, P., Teng, S. W., Murshed, M., Pang, S., Li, Y. and Lin, H., *Crop monitoring by multimodal remote sensing: a review*, Remote Sens. Appl.: Soc. Environ. (2023), 101093.

[12] Khan, H. A., Khan, M. M., Khurshid, K. and Chanussot, J., *Saliency based visualization of hyper-spectral images*, 2015 IEEE International Geoscience and Remote Sensing Symposium. Proc. of IGARSS 2015, Milan, Italy, July 26-31, 2015, IEEE, 1096-1099, 2015.

[13] Le Moan, S., Mansouri, A., Voisin, Y. and Hardeberg, J. Y., *A constrained band selection method based on information measures for spectral image color visualization*, IEEE Trans. Geosci. Remote Sens. **49** (2011), no. 12, 5104-5115.

[14] Lechner, A. M., Foody, G. M. and Boyd, D. S., *Applications in remote sensing to forest ecology and management*, One Earth **2** (2020), no. 5, 405-412.

[15] Lei, T., Wang, J., Li, X., Wang, W., Shao, C. and Liu, B., *Flood disaster monitoring and emergency assessment based on multi-source remote sensing observations*, Water **14** (2022), no. 14, 2207.

[16] Li, J., Pei, Y., Zhao, S., Xiao, R., Sang, X. and Zhang, C., *A review of remote sensing for environmental monitoring in China*, Remote Sens. **12** (2020), no. 7, 1130.

[17] Mahajan, U. and Bundel, B. R., *Drones for normalized difference vegetation index (NDVI), to estimate crop health for precision agriculture: a cheaper alternative for spatial satellite sensors*, Proc. of Int. Conf. on Innovative Research in Agriculture, Food Science, Forestry, Horticulture, Aquaculture, Animal Sciences, Biodiversity, Ecological Sciences and Climate Change (AFHABEC-2016), Delhi, India, 2016, 31, 2016.

[18] Mittal, A., Moorthy, A. K. and Bovik, A. C., *No-reference image quality assessment in the spatial domain*, IEEE Trans. Image Process. **21** (2012), no. 12, 4695-4708.

[19] OpenWeather, *Visualisation of the NDVI index on satellite maps. Custom palettes for agricultural applications*, Available at https://openweathermap.medium.com/visualisation-of-the-ndvi-index-on-satellite-maps-custom-palettes-for-agricultural-applications-f99b0652f991 (2023/08/04).

[20] Pettorelli, N., *The normalized difference vegetation index*, Oxford University Press, USA, 2013.

[21] Phang, S. K., Chiang, T. H. A., Happonen, A. and Chang, M. M. L., *From satellite to UAV-based remote sensing: a review on precision agriculture*, IEEE Access (2023).

[22] Plajer, I. C., Baicoianu, A. and Majercsik, L., *AI-based visualization of remotely-sensed spectral images*, 2023 International Symposium on Signals, Circuits and Systems. Proc. of ISSCS 2023, Iasi, Romania, July 13-14, 2023, IEEE, 1-4, 2023.

[23] Plajer, I. C., Baicoianu, A., Majercsik, L. and Ivanovici, M., *Multisource remote sensing data visualization using machine learning*, IEEE Trans. Geosci. Remote Sens. (2024).

[24] Plajer, I. C., Baicoianu, A., Majercsik, L. and Ivanovici, M., *NDVI computation from hyperspectral images*, 13th Workshop on Hyperspectral Image and Signal Processing: Evolution in Remote Sensing. Proc. of WHISPERS 2023, Athens, Greece, Oct 31 - Nov 2, 2023, IEEE, 2023.

[25] Rodriguez-Veiga, P., Quegan, S., Carreiras, J., Persson, H. J., Fransson, J. E., Hoscilo, A., Ziolkowski, D., Sterenczak, K., Lohberger, S., Stangel, M. et al., *Forest biomass retrieval approaches from earth observation in different biomes*, Int. J. Appl. Earth Obs. Geoinf. **77** (2019), 53-68.

[26] Shimoni, M., Haelterman, R. and Perneel, C., *Hypersectral imaging for military and security applications: combining myriad processing and sensing techniques*, IEEE Geosci. Remote Sens. Mag. **7** (2019), no. 2, 101-117.

[27] Silleos, N. G., Alexandridis, T. K., Gitas, I. Z. and Perakis, K., *Vegetation indices: advances made in biomass estimation and vegetation monitoring in the last 30 years*, Geocarto Int. **21** (2006), no. 4, 21-28.

[28] Su, H., Du, Q. and Du, P., *Hyperspectral image visualization using band selection*, IEEE J. Sel. Top. Appl. Earth Obs. Remote Sens. **7** (2013), no. 6, 2647-2658.

[29] Su, H., Wu, Z., Zhang, H. and Du, Q., *Hyperspectral anomaly detection: a survey*, IEEE Geosci. Remote Sens. Mag. **10** (2022), no. 1, 64-90.

[30] Thenkabail, P. S., Smith, R. B. and De Pauw, E., *Hyperspectral vegetation indices and their relationships with agricultural crop characteristics*, Remote Sens. Environ. **71** (2000), no. 2, 158-182.

[31] Tu, B., Yang, X., Zhou, C., He, D. and Plaza, A., *Hyperspectral anomaly detection using dual window density*, IEEE Trans. Geosci. Remote Sens. **58** (2019), no. 12, 8503-8517.

[32] Weiss, M., Jacob, F. and Duveiller, G., *Remote sensing for agricultural applications: a meta-review*, Remote Sens. Environ. **236** (2020), 111402.

[33] Wellmann, T., Lausch, A., Andersson, E., Knapp, S., Cortinovis, C., Jache, J., Scheuer, S., Kremer, P., Mascarenhas, A., Kraemer, R. et al., *Remote sensing in urban planning: contributions towards ecologically sound policies?*, Landscape Urban Plan. **204** (2020), 103921.

[34] Yasuma, F., Mitsunaga, T., Iso, D. and Nayar, S. K., *Generalized assorted pixel camera: postcapture control of resolution, dynamic range, and spectrum*, IEEE Trans. Image Process. **19** (2010), no. 9, 2241-2253.

[35] Yin, J., Dong, J., Hamm, N. A., Li, Z., Wang, J., Xing, H. and Fu, P., *Integrating remote sensing and geospatial big data for urban land use mapping: a review*, Int. J. Appl. Earth Obs. Geoinf. **103** (2021), 102514.

[36] Yuan, Q., Shen, H., Li, T., Li, Z., Li, S., Jiang, Y., Xu, H., Tan, W., Yang, Q., Wang, J. et al., *Deep learning in environmental remote sensing: achievements and challenges*, Remote Sens. Environ. **241** (2020), 111716.

[37] Zhang, L., Ji, L. and Wylie, B. K., *Response of spectral vegetation indices to soil moisture in grasslands and shrublands*, Int. J. Remote Sens. **32** (2011), no. 18, 5267-5286.

[38] Zhang, T., Cai, Y., Zhuang, P. and Li, J., *Remotely sensed crop disease monitoring by machine learning algorithms: a review*, Unmanned Syst. **12** (2024), no. 1, 161-171.

[39] Zhang, Z., Fang, Y., Yan, J. and Du, R., *No-reference quality assessment for realistic distorted images by color moment and texture features*, 2020 IEEE Conference on Multimedia Information Processing and Retrieval. Proc. of MIPR 2020, Shenzhen, China, August 6-8, 2020, IEEE, 342-347, 2020.

[40] Ziemann, A., Simonoko, H. and Flynn, E., *Temporal anomaly detection in multispectral imagery*, 2020 IEEE International Geoscience and Remote Sensing Symposium. Proc. of IGARSS 2020, Waikoloa, HI, USA, Sept 26 - Oct 2, 2020, IEEE, 3975-3978, 2020.